

1 Ontogenetic and *in-silico* models of
2 spatial-packing in the hypermuscular
3 mouse skull

4
5 N. S. Jeffery¹, D. Sarver^{2,3} and C.L. Mendias^{2,4}

6
7 1. Institute of Life Course & Medical Sciences, University of Liverpool, UK

8 2. Department of Orthopaedic Surgery, University of Michigan, USA

9 3. School of Medicine, Johns Hopkins University, USA

10 4. HSS Research Institute, Hospital for Special Surgery, USA

11
12
13
14
15
16
17
18
19
20
21
22
23
24
25
26 **Keywords:** spatial-packing, masseter, endocranial, myostatin, mouse

30
31
32
33
34
35
36
37
38
39
40
41
42
43
44
45
46
47
48
49
50
51
52
53
54
55
56
57
58
59
60
61
62
63
64
65
66
67
68

Abstract

Networks linking single genes to multiple phenotypic outcomes can be founded on local anatomical interactions as well as on systemic factors like biochemical products. Here we explore the effects of such interactions by investigating the competing spatial demands of brain and masticatory muscle growth within the hypermuscular myostatin deficient mouse model and in computational simulations. Mice that lacked both copies of the myostatin gene (-/-) and display gross hypermuscularity, and control mice that had both copies of the myostatin gene (+/+) were sampled at 1, 7, 14 and 28 postnatal days. A total of 48 mice were imaged with standard as well as contrast-enhanced microCT. Size metrics and landmark configurations were collected from the image data and were analysed alongside *in-silico* models of tissue expansion. Findings revealed that: masseter muscle volume was smaller in -/- mice at 1 day but became, and remained thereafter, larger by 7 days; -/- endocranial volumes begin and remained smaller; -/- enlargement of the masticatory muscles was associated with caudolateral displacement of the calvarium, lateral displacement of the zygomatic arches, and slight dorsal deflection of the face and basicranium. Simulations revealed basicranial retroflexion (flattening) and dorsal deflection of the face associated with muscle expansion and abrogative covariations of basicranial flexion and ventral facial deflection associated with endocranial expansion. Our findings support the spatial-packing theory and highlight the importance of understanding the harmony of competing spatial demands that can shape and maintain mammalian skull architecture during ontogeny.

69

70

71 **Introduction**

72 Anatomical structures physically interact to varying degrees throughout ontogeny, adulthood,
73 and evolution. During ontogeny, genetically mediated changes in one structure can
74 simultaneously affect important epigenetic changes in several surrounding structures.
75 Moreover, interactions that reliably generate the same or similar phenotypes over successive
76 ontogenies can shield from selection mutations in genes that would have otherwise
77 predominantly shaped those affected structures (see Green et al., 2017; Zheng et al. 2019;
78 Lahti et al., 2009). These mutations can then accumulate, leading to punctuated phenotypic
79 diversification as conditions prevail that destabilise the protective network of interactions and
80 expose the gene variants to selection (Gould, 2002; Laland et al., 2015). Interactions also
81 allow for phenotypic adjustments during life, which can accommodate behavioural changes
82 of, for example, dietary niche or physical activity (e.g. Anderson et al., 2014). This capability
83 extends into adulthood and can help genetically similar individuals and populations to tolerate
84 and thrive under different environmental conditions (see Murren et al, 2015). The premise that
85 structural interactions help define and maintain morphological outcomes has a long history
86 and has taken many forms over the decades (e.g. Kappers, 1932; Neubauer, 1925;
87 Weidenreich, 1941; Weiss, 1933; Wolff, 1893). Most relevant to this paper are paradigms that
88 define specific, typically spatially co-ordinated networks of interactions such as the functional
89 matrix hypothesis formulated by Moss (Moss & Young, 1960) and its derivative, the spatial-
90 packing hypothesis popularised by Ross (Ross & Ravosa, 1993). More recently, the concept
91 has also become implicit to theories of morphological integration and modularity (e.g.
92 Goswami et al., 2015; Klingenberg, 2014). Here we explore the spatial-packing hypothesis.

93 The central tenet of the spatial-packing hypothesis is that the head has a finite capacity to
94 accommodate and maintain the functional integrity of a range of structures. Once spatially
95 optimised, any subsequent relative expansion of one structure necessitates changes of form
96 or function of one or more of its neighbouring structures. Lesciotto and Richtsmeier (2019)
97 offer an excellent comprehensive review of the core principles (see also Lieberman et al.,
98 2000; Singleton, 2013). Expansion of the brain is most often studied in this context, particularly
99 amongst highly encephalised primates. There is substantial empirical evidence from adult
100 interspecific studies and from the fossil record to support the notion that the primate skull,
101 particularly the basicranium and face as well as the neurocranium, changed shape to fit
102 relative expansion of the brain (e.g. Ross & Ravosa, 1993; Ross & Henneberg, 1995; Bastir
103 et al., 2010). An often-cited competing spatial demand to brain expansion is the relative size
104 of the masticatory apparatus. Biegert (1963) was first to outline this trade-off, suggesting that
105 expansion of the masticatory apparatus relative to the brain constrains brain-related changes
106 of the skull. Again, there is strong support from adult interspecific studies as well as the fossil
107 record (e.g. Ross & Ravosa, 1993; Ross & Henneberg, 1995; Veneziano et al. 2019; Neaux
108 et al., 2015). The mechanism(s) by which the skull responds to such competing spatial
109 demands during ontogeny are unclear. It seems likely that strain gradients created by
110 expanding tissues trigger cellular activity and incremental architectural remodelling (see
111 Enlow, 1962 and, for example, more recently Edamoto et al. 2019). However, whilst the
112 mechanotransduction of muscle and kinematic forces is well documented (see reviews by
113 Stewart et al., 2020; Vincent & Wann, 2019), we know comparatively little about the efficacy
114 of the low amplitude and low frequency stimuli elicited by tissue expansion. Another, congruent
115 agent could be straightforward mechanical deformation –skull features are shaped and held
116 in place by tissue growth in a way that is defined by the geometry, relative rigidity and spatial

117 relationships of the tissues involved. This is reminiscent of the analogy popularised by Enlow
118 (1976), and others, in which an inflating balloon bends around a piece of tape adhered to its
119 surface.

120

121 Here we evaluate the potential of simple mechanical deformation to describe changes of skull
122 shape and we also test Biegert's spatial-packing hypothesis using a myostatin (GDF-8) knock-
123 out mouse model of hypermuscularity. Myostatin is a member of the transforming growth
124 factor-beta (TGF- β) superfamily and acts as a negative regulator of skeletal muscle growth in
125 vertebrates. It signals via type IB and IIB activin receptors to inhibit muscle progenitor cell
126 proliferation, activate proteolytic systems, and inhibit protein synthesis in the mature muscle.
127 A loss of the gene encoding myostatin results in a greatly increased skeletal muscle mass, via
128 fiber hypertrophy and hyperplasia (Mendias et al., 2006). Previous studies have shown
129 significant increases of masseter mass among myostatin knock-out (-/-) mice in adults and at
130 a range of ontogenetic time-points (e.g. Cray et al, 2011; Vecchione et al, 2010). Volumes
131 reported by Jeffery & Mendias (2014) further confirmed masseter enlargement and revealed
132 for the first time an associated reduction of brain size.

133 We use the latest advances of contrast-enhanced microCT, non-Euclidean geometric
134 morphometrics as well as computational tissue modelling to test for shape changes that co-
135 vary with enlargement of the masticatory muscles relative to brain size during ontogeny. Our
136 spatial-packing hypothesis has two parts. The first part states that masticatory muscle
137 enlargement constrains brain growth as implied by Stedman et al (2004) (see also Anthony,
138 1903). This predicts a close association between the ontogenetic timing of hypermuscularity
139 and the reduced brain size seen in adult -/- mice. The second part follows Biegert's (1963)
140 proposal that relative masticatory muscle enlargement constrains the effects of brain growth
141 on the surrounding skull. This predicts that skull markers of brain expansion, such as base
142 flexion and klinorhynch (ventral facial deflection), are diminished among -/- mice. However,
143 in our -/- mouse model the spatial-packing problem of enlarged musculature is conflated with
144 reduced brain size, possibly due to suppressed myostatin expression within the brain (see
145 Discussion), and with the structural effects of increased muscle and bite force (e.g. Byron et
146 al., 2006; Williams et al, 2015). We therefore inferred the extricated and combined effects of
147 brain and muscle growth on skull architecture *in-silico* and in doing so we also evaluate the
148 ability of simple deformation to describe spatial-packing related phenomena. Simulations were
149 evaluated empirically with reference to previously published observations notionally linked to
150 spatial-packing. Predictions included: basicranial flexion and ventral facial deflection
151 associated with simulated brain expansion (e.g. e.g. Ross & Ravosa, 1993); basicranial
152 flattening and dorsal facial deflection (airorhynch) associated with simulated muscle
153 expansion (e.g. Ross & Henneberg, 1995); diminished basicranial flexion and diminished
154 ventral facial deflection associated with simulated brain and muscle expansion (e.g. Biegert,
155 1963).

156

157 **Methods**

158 *Sample:* Control (+/+) and myostatin deficient (-/-) mice on a C57BL/6J background were
159 reared and culled at the University of Michigan in strict accordance with Institutional Animal
160 Care & Use Committee approval (PRO6079). Mice share a common maternal genotype and
161 both sets of parents and offspring were reared under standardised laboratory conditions. A
162 total of 48 male mice were sampled at 1, 7, 14 & 28 postnatal days (6 +/+ and 6 -/- per age
163 group). Heads were removed post-mortem and fixed in 10% neutral buffered formalin.

164 Genotype of mice was determined by isolating DNA from tail biopsies and PCR-based
165 detection of the wild type *Mstn* (+) and knock-out *Mstn* (-) alleles as described by Mendias et
166 al. (2006). Sex was confirmed using PCR probes against the *Sry* gene, which is located on
167 the Y chromosome.

168 *Imaging:* Each head was imaged twice. Once with standard microCT to capture the skull
169 geometry and subsequently with I₂KI (9% w/v) enhanced microCT to visualise the muscle
170 architecture (see Fig. 1 and Jeffery et al, 2011). Both sets were acquired using a SkyScan
171 1272 (Bruker Ltd) with 50Kv, 200uA and an aluminium filter. Vertices of the resulting
172 isometric voxels ranged from 26 to 40um. Contrast enhancement is associated with tissue
173 shrinkage (Vickerton et al., 2013). The method was standardised here so the effect is likely
174 to be the same for both groups and small given findings from similar whole mouse head
175 studies (e.g. Cox & Jeffery, 2011; Baverstock et al., 2013; Jeffery & Mendias, 2014).

176 *Morphometrics:* Masseter muscle and endocranial volumes were calculated using the
177 stereological method implemented in VolumEst (v2010) for ImageJ (v1.51p). The
178 endocranium is a reliable proxy for the brain in a range of craniates, including mammals (e.g.
179 Dumoncel et al., 2020; Early et al., 2020). Relative masseter size was calculated as
180 masseter volume divided by endocranial volume. Skull centroid size was calculated as the
181 square root of the sum of squared distances between the landmarks shown in Figure 2a.
182 Bivariate plots with local estimated scatterplot smoothing (LEOSS) and boxplots with
183 Wilcoxon comparisons of -/- and +/+ means were created in R (version 3.6.2). Three-
184 dimensional co-ordinates for a configuration of 18 reliable and readily identifiable skull
185 landmarks (Fig. 2a) were collected using the mark-up function in 3DSlicer (v4.10.1). This
186 configuration was chosen to provide reasonable morphological representation whilst keeping
187 the dimensionality of the shape space ($3L-7 = 47$) proportionate to the sample size (48) (see
188 Bookstein, 2017, 2019; Cardini, 2019; Cardini et al, 2019). Geometric morphometric
189 variations of the configuration of landmarks were investigated in MorphoJ (v1.07a) following
190 the principles and methods outlined by Drake & Klingenberg (2008) and Klingenberg (2016).
191 Allometric (size) related shape changes were investigated using a multivariate regression of
192 symmetric Procrustes coordinates against log-transformed centroid size. Residuals from this
193 regression were explored for nonallometric shape changes. Differences across age cohorts
194 and experimental groups were evaluated in MorphoJ with Canonical Variate Analysis (CVA)
195 and Discriminative Functions of Procrustes coordinates. Warped surfaces were created in
196 Landmark (version 3.0) with reference to the co-ordinates generated by MorphoJ. For
197 convenience, we illustrated the distribution of simulated forms within their own shape space
198 using a Principal Components Analysis (PCA) of the covariance matrix and crossed checked
199 findings against those generated by mesh deformations (see below).

200 *Computational simulation:* Deformations of the skull due to endocranial and muscle
201 enlargement were simulated *in-silico* using a mass exchange gradient finite element
202 approach (see Ateshian et al 2009). Co-registered standard and contrast enhanced microCT
203 data (Fig. 2b) for the control (+/+) 28 day mouse closest to the mean shape (specimen
204 M1C1) were used to reconstruct, refine and mesh a model of the skull, mandible and
205 masticatory muscles (masseter, temporalis and pterygoids) in Amira version 5.4.1 (Thermo
206 Fisher Scientific ltd, Waltham, Massachusetts, USA). The final decimated tetrahedral mesh,
207 which consisted of 1.3 million elements (Fig. 2c), was imported into FEBio version 2.8.2
208 (Maas et al., 2012) and parameterised. The simulation was simplified by assuming the skull
209 was a structural continuum and that skull elasticity was invariant spatially as well as for the
210 duration of the simulation. The mandibular incisors were used as rigid body constraints, and
211 the mass exchange gradients representing constituent materials were adjusted to achieve
212 the desired volumetric changes relative to the baseline +/+model (S_{+/+}). One model was

213 created to simulate the 28 day -/- condition ($S_{-/-}$). In this case, the $S_{+/+}$ baseline model
214 elastically deforms to accommodate a computationally driven 7% reduction of endocranial
215 volume and 17% increase of masticatory muscle volume. This was repeated without the
216 endocranial reduction (M_{+17}). The remaining simulations were used to explore shape
217 changes associated with theoretical expansion of the muscles and endocranium (see Table
218 1). The models were solved using a non-linear quasi-static method, landmarked and
219 incorporated into the shape analyses as outlined above. Whole mesh deformations were
220 also visualised in FEBio.

221 In all statistical comparisons a probability (p) value of ≤ 0.05 was used to identify the most
222 prominent differences. Although somewhat arbitrary and subject to recent criticism (e.g.
223 Amrhein et al., 2019), this threshold was appropriate for the purposes of this study on the
224 understanding that a $p > 0.05$ is not equivalent to no difference but can represent a weaker
225 effect compared with ≤ 0.05 .

226

227 **Results**

228 *Euclidean Morphometrics*: Bivariate plots against age with accompanying boxplots and
229 Wilcoxon p-values are given in Figures 3a-d. Endocranial volumes were larger in +/+ mice
230 from 1 through to 28 postnatal days (Fig3a). Masseter volumes were at first larger among
231 the +/+ mice (1 day), switching to larger among -/- mice at 7 and 28 days (Fig3b). By 28
232 days -/- masseters and endocrania were on average 17% larger and 7% smaller,
233 respectively. Both groups experienced increased relative masseter size (masseter
234 volume/endocranial volume) after day 7 (Fig. 3c). The increase was greater for -/- mice.
235 There was little difference of centroid size until 28 days, at which point +/+ mice were on
236 average 1.1mm larger (Fig 3d). These findings predict corresponding shifts of skull form to
237 accommodate relative masticatory muscle enlargement, and that such effects will be more
238 pronounced among the -/- mice.

239 *Geometric Morphometrics*: Regression (Fig. 4a) of the symmetric component of the
240 Procrustes co-ordinates (combined fit; $n=48$) suggests both -/- and +/+ mice follow a
241 common allometric trend against centroid size, which explains approximately 77% of the
242 total shape variation. Allometric changes from 1 to 28 days are illustrated in Figure 4b and
243 included relative: elongation of the palate; narrowing of the midface and calvarium; flattening
244 of the posterior cranial base and ventrodorsal shortening of the calvarium. Overall, the mean
245 skull shape representative of all 28day mice was relatively more compact and
246 dolichocephalic whilst the face was longer and deflected dorsally (airorhynch).

247 Relative masseter size predicted 59% (p-value < 0.001) of the shape variation from 1 to 28
248 days. It also predicted 17% of the shape variance after size correction (residuals of
249 regression against centroid size). Figure 3c suggested relative masseter enlargement
250 occurred after day 1. Limiting the current analyses to days 7 to 28 showed that relative
251 masseter size predicted 48% of the nonallometric shape variance (Figure 5a). Changes
252 described included relative lateral displacement of the zygomatic arches, elongation of the
253 face, as well as narrowing and ventrodorsal shortening of the neurocranium and slight dorsal
254 bending of the face and of the posterior cranial base (Fig.5b). These patterns were broadly
255 similar to the allometric shape changes shown in Figure 4b, reflecting shared groupings
256 according to development (age) as well as growth (size).

257 Canonical Variate Analysis (CVA) of size corrected data revealed partitioning of the
258 nonallometric shape space between -/- and +/+ mice across canonical variate 2, which
259 represented 19% of the total variance (Fig. 6a). Procrustes distances are given in Table 2.

260 Shape differences at 28 days shown in Figure 5b were drawn from a discriminative function
261 (Procrustes D = 0.0271, $p < 0.0001$; cross-validation 100% accurate assignment). The major
262 shape differences were lateral displacement of the arches and caudolateral expansion of the
263 neurocranium among the 28 day $-/-$ mice. Also observed in $-/-$ mice were a decrease of facial
264 height, particularly around the rostrum, and slight dorsal deflection of the palate.

265

266 *Simulations:* Computational simulations are summarised in Table 1. To evaluate our
267 approach, the simulations of the control model ($S_{+/+}$) and those approximating the $-/-$
268 condition at 28 days ($S_{-/-}$ & M_{+17}) were combined with the main dataset and the CVA reported
269 above was repeated. Figure 6c shows the equivalent plot including the control simulation
270 ($S_{+/+}$), which clusters with the 28 day $+/+$ mice. Shape differences described by the variates
271 are the same in both analyses. The simulated 17% muscle expansion (M_{+17}) and muscle
272 expansion plus 7% endocranial reduction ($S_{-/-}$) models both cluster with the $-/-$ mice (please
273 refer to Table 1 for abbreviations and conditions). These findings confirmed that simulations
274 broadly mimic actual shape differences observed between $-/-$ and $+/+$ mice (see above) and
275 indicated that muscle enlargement rather than reduced endocranial growth had the greatest
276 influence on these shape differences.

277 The three empirically informed simulations ($S_{+/+}$, $S_{-/-}$ & M_{+17}) were then combined with
278 extended, theoretical, models of muscle and endocranial expansion (see Table 1) and
279 subjected to PCA. PC1 explained 94% of variance (Fig. 7a), representing mostly simulated
280 increases of masticatory muscle volume in one direction (+PC) and simulated increases of
281 endocranial volume in the other (-PC). Simulated enlargement of the masticatory muscles
282 was associated with lateral displacement of the zygomatic arches, dorsal deflection of the
283 face (airorhynch), ventrodorsal shortening of the neurocranium, and retroflexion (flattening)
284 of the posterior cranial base (Fig. 7b). The opposite trend was seen with simulated
285 endocranial enlargement (Fig. 7c), which was characterised by basicranial flexion,
286 neurocranial enlargement and ventral deflection of the face (kyphosis or klinorhynch). PC2
287 (6%) showed the combined effects of computationally driven muscle and endocranial
288 expansion. Findings indicate that muscle expansion limits endocranial induced flexion of the
289 posterior cranial base and endocranial expansion limits dorsal deflection of the face
290 associated with muscle enlargement (Fig. 7d). Whole mesh (1.3 million elements)
291 displacement vector plots (bottom row in Figs. 7b-d) revealed similar trends to the above
292 landmarked defined analyses. Endocranial expansion was primarily characterised by
293 neurocranial expansion as well as ventral deflection of the face and the cranial base,
294 including basicranial flexion (bottom row Fig. 7c). By contrast, muscle expansion was
295 primarily characterised dorsal deflection of the posterior neurocranium, face and cranial
296 base, including basicranial retroflexion, as well as lateral expansion of the zygomatic arches
297 (bottom row Fig. 7b). Combining the two simulated expansions, appears to redirect and
298 magnify the displacement posteriorly whilst constraining the flexion to basicranial elongation
299 and the extent of dorsal facial deflection (bottom row Fig. 7d). Lateral displacement of the
300 zygomatic arches remained.

301

302 **Discussion**

303 Compared with the controls ($+/+$), the 28-day old myostatin deficient ($-/-$) mice had on
304 average 17% larger masseters and 7% smaller endocrania, the latter being used here as a
305 proxy for brain size (see methods). A previous study by Jeffery & Mendias (2014) suggests
306 this pattern continues into later adulthood with differences of +43% and -16%, respectively in

307 mice aged 60 to 517 days (average 233 days). Similar increases of masseter size have been
308 reported before (see Vecchione et al., 2007 & 2010; Cray et al 2011). In particular, our
309 results corroborate those of Vecchione et al (2010) showing that day old +/- mice have
310 larger masseters than -/- mice. These findings suggest that the hypermuscular phenotype
311 emerges after birth, during the first week of life, and then rapidly accelerates. By contrast,
312 the -/- mice had smaller endocrania from day one, which suggests the reduced brain size
313 occurred in-utero and preceded and then accompanied the accelerated muscle growth.
314 Thus, our findings do not corroborate the idea of muscularity directly constraining brain size
315 as implied by Stedman et al (2004). Indeed, that -/- endocrania are smaller at birth suggests
316 the involvement of more systemic factors.

317 Myostatin is known to be an important pre- and postnatal metabolic regulator (McPherron
318 and Lee, 2002; Guo et al, 2009; Ploquin et al, 2012; Carneiro et al, 2013; Mouisel et al,
319 2014) and has been shown to act as a communicative link between muscle and fat (Kong et
320 al, 2018; Deng et al, 2020). Deficiency may therefore limit the availability of lipids for myelin
321 formation, which can in turn impede intra-uterine brain growth (Bourre et al., 1981; Morand
322 et al., 1981). Myostatin deficiency may also have altered brain cell development. Since we
323 reported the reduced endocranial phenotype in 2014, several studies have reported the
324 abundant expression of myostatin-like proteins throughout the brain, including glia as well as
325 neurons (e.g. Hayashi et al, 2018; Schafer et al, 2019; Augustin et al., 2017). This suggests
326 myostatin is an important factor for neuronal growth and maintenance. We therefore contend
327 that the reduced -/- endocrania reported here and by Jeffery and Mendias (2014) are the
328 product of altered prenatal neuronal growth, possibly exacerbated by the metabolic demands
329 of growing and maintaining larger muscles later in life.

330 Rather than constraining brain size, our mouse data and more clearly our simulations
331 support the hypothesis that masticatory muscle enlargement limits the effects of brain
332 expansion on the surrounding skull. Most notably, masticatory muscle enlargement curbs
333 basicranial flexion, whilst brain enlargement in turn restricts some effects of muscle
334 enlargement such as dorsal deflection of the face (Biegert, 1963; see also Ross & Ravosa,
335 1993; Ross & Henneberg, 1995). The aim of our computational approach was not to
336 replicate the intricacies of the murine head but to simulate deformation driven by tissue
337 expansion. Realism could and should be enhanced in future models, albeit at the expense of
338 computational load and possibly stability. Refinements might include, for example, growth of
339 additional anatomical modules such as the eyes and extraocular apparatus (e.g. Ross &
340 Kirk, 2007; Jeffery et al., 2007), nuchal musculature and nasal turbinates as well as the face
341 (Bastir et al., 2010), the pharynx (e.g. Jeffery, 2005) and the nasal septum (Jeffery et al.,
342 2007). Adding ontogenetic shifts of skull compliance will be particularly enlightening,
343 especially changes related to the formation of ossification centres and the subsequent
344 localisation of deformation to, and eventual fusion of, sutures and synchondroses (see
345 Michejda, 1972; Jeffery & Spoor, 2004; Oladipupo et al., 2020). Whilst adding such
346 complexity will no doubt provide more detail and nuance (see for example Lee &
347 Richtsmeier, 2019), it is remarkable nonetheless how much of the *in-vivo* changes were
348 captured here *in-silico* on the basis of simply tissue expansion and elastic deformation.
349 Mechanical deformation appears to mirror the effects of mechanisms underlying ontogeny of
350 the murine skull and is perhaps a precursor or adjunct to physiological tissue (re)modelling.

351 From these and previous findings we can infer the variegated and phasic nature of skull
352 ontogeny (see also Bastir and Rosas 2016; Zollikofer et al. 2017). We know that
353 morphogenetic covariations predominate during embryogenesis. Presumably, these trends
354 remain coherent for most of prenatal life, reflecting the residual power of the genes involved
355 as well as relatively relaxed functional demands and spatial constraints. For example,

356 consider the fetus suspended in amniotic fluid, nourished via the umbilical cord and with a
357 flexible, membranous, calvarium. Recent in-utero MR images have also shown a
358 comfortable margin of cerebrospinal fluid surrounding the brain, which could be displaced via
359 arachnoid granulations to lessen the physical effects of encephalisation on the surrounding
360 skull (see figures in Jarvis et al, 2019; Kyriakopoulou et al., 2017). In other words, the head
361 is not yet spatially optimised at this stage and retains capacity to accommodate expanding
362 tissues. However, as ontogeny proceeds, the genetic signals lose coherence, developmental
363 noise accumulates and tissues become increasingly crowded and sculpted by functional
364 demands like mastication. At this point, the established spatial arrangement of tissues,
365 referred to here as heterotopy, would be distorted by greater competition for space as
366 modules adopt distinct allometric trajectories and disperse along different heterochronic
367 timelines (see Zelditch & Fink 1996; Zollikofer & Ponce De León, 2004). This supposition,
368 which is summarised in Figure 8, might help explain why investigations of spatial-packing
369 using fetal samples (e.g. Jeffery & Spoor, 2002 & 2004; Jeffery, 2003; Jeffery et al., 2007)
370 have seemingly contradicted adult studies (e.g. Ross & Ravosa, 1993; Ross & Henneberg,
371 1995; Veneziano et al. 2019; Neaux et al., 2015). Indeed, whilst it pains at least one of us
372 (NJ) to concede, it appears that spatial-packing like phenomena are best detected later in
373 ontogeny and possibly in differences among the adult, spatially optimised, endpoints rather
374 than along intraspecific prenatal ontogenies. The above paradigm also emphasises the
375 importance of considering the protean mix of sources as well as the resulting patterns of
376 covariation in studies of morphological integration and modularity over ontogenetic time
377 (Klingenberg, 2008; 2014), and supports the case for explicitly recognising spatial-packing
378 like covariations linked to heterotopy in the various theoretical frameworks that govern such
379 studies and our current understanding of mammalian skull development.

380

381 **Acknowledgements**

382 The authors would like to thank the many developers involved in creating and maintaining
383 FEBio (www.febio.org), R (www.r-project.org), 3Dslicer (www.slicer.org) as well as MorphoJ
384 (www.morphometrics.uk) and ImageJ (imagej.nih.gov). Without their support this research
385 would not have been financially viable. We also thank two reviewers for their comments and
386 suggestions. Thanks to their input, the final version of this manuscript is a significant
387 improvement on the original submitted.

388

389 **Conflicts of Interest**

390 None declared

391 **Data availability statement**

392 All relevant data are presented in the results section and figures.

393

394

395

396 **ORCID**

397 Nathan Jeffery <https://orcid.org/0000-0001-5166-2029>

398 Christopher Mendias <https://orcid.org/0000-0002-2384-0171>

399

400

401 **References**

402 Amrhein, V., Greenland, S., & McShane, B. (2019). Comment: Retire statistical significance.
403 Nature, 567, 305-307.

404 Anderson, P. S., Renaud, S., & Rayfield, E. J. (2014). Adaptive plasticity in the mouse
405 mandible. BMC Evolutionary Biology, 14(1), 85.

406 Anthony, R. (1903). Introduction à l'étude expérimentale de la morphogénie. Bulletins et
407 Mémoires de la Société d'Anthropologie de Paris, 4(1), 119-145.

408 Ateshian, G. A., Costa, K. D., Azeloglu, E. U., Morrison, B., & Hung, C. T. (2009). Continuum
409 modeling of biological tissue growth by cell division, and alteration of intracellular osmolytes
410 and extracellular fixed charge density. *Journal of biomechanical engineering*, 131(10),
411 101001.

412 Augustin, H., McGourty, K., Steinert, J. R., Cochemé, H. M., Adcott, J., Cabecinha, M., &
413 Partridge, L. (2017). Myostatin-like proteins regulate synaptic function and neuronal
414 morphology. *Development*, 144(13), 2445-2455.

415 Bastir, M., Rosas, A., Stringer, C., Cuétara, J. M., Kruszynski, R., Weber, G. W., ... &
416 Ravosa, M. J. (2010). Effects of brain and facial size on basicranial form in human and
417 primate evolution. *Journal of Human Evolution*, 58(5), 424-431.

418 Bastir M, and Rosas A. 2016. Cranial base topology and basic trends in the facial evolution
419 of Homo. *Journal of Human Evolution* 91:26-35.

420 Baverstock, H., Jeffery, N. S., & Cobb, S. N. (2013). The morphology of the mouse
421 masticatory musculature. *Journal of Anatomy*, 223(1), 46-60.

422 Biegert, J. (1963). The evaluation of characteristics of the skull, hands and feet for primate
423 taxonomy. In *Classification and human evolution* (Vol. 37, pp. 116-145). Aldine Chicago.

424 Bookstein, F. L. (2017). A newly noticed formula enforces fundamental limits on geometric
425 morphometric analyses. *Evolutionary Biology*, 44(4), 522-541.

426 Bookstein, F. L. (2019). Pathologies of between-groups principal components analysis in
427 geometric morphometrics. *Evolutionary Biology*, 46(4), 271-302.

428 Bourre, J. M., Morand, O., Chanez, C., Dumont, O., & Flexor, M. A. (1981). Influence of
429 intrauterine malnutrition on brain development: alteration of myelination. *Neonatology*, 39(1-
430 2), 96-99.

431 Byron, C. D., Hamrick, M. W., & Wingard, C. J. (2006). Alterations of temporalis muscle
432 contractile force and histological content from the myostatin and Mdx deficient mouse.
433 *Archives of oral biology*, 51(5), 396-405.

434 Cardini, A. (2019). Integration and modularity in Procrustes shape data: is there a risk of
435 spurious results?. *Evolutionary Biology*, 46(1), 90-105.

- 436 Cardini, A., O'Higgins, P., & Rohlf, F. J. (2019). Seeing distinct groups where there are none:
437 spurious patterns from between-group PCA. *Evolutionary Biology*, 46(4), 303-316.
- 438 Carneiro, I., González, T., López, M., Señarís, R., Devesa, J., & Arce, V. M. (2013).
439 Myostatin expression is regulated by underfeeding and neonatal programming in rats.
440 *Journal of physiology and biochemistry*, 69(1), 15-23.
- 441 Cox, P. G., & Jeffery, N. (2011). Reviewing the morphology of the jaw-closing musculature in
442 squirrels, rats, and guinea pigs with contrast-enhanced microCT. *The Anatomical Record:*
443 *Advances in Integrative Anatomy and Evolutionary Biology*, 294(6), 915-928.
- 444 Cray Jr, J., Kneib, J., Vecchione, L., Byron, C., Cooper, G. M., Losee, J. E., ... & Mooney, M.
445 P. (2011). Masticatory HyperMuscularity is not Related to Reduced Cranial Volume in
446 Myostatin-Knockout Mice. *The Anatomical Record: Advances in Integrative Anatomy and*
447 *Evolutionary Biology*, 294(7), 1170-1177.
- 448 Deng, B., Zhang, F., Wen, J., Shen, W., Gao, Q., Peng, X., ... & Liu, W. (2020). The
449 transcriptomes from two adipocyte progenitor cell types provide insight into the differential
450 functions of MSTN. *Genomics*.
- 451 Drake, A. G., & Klingenberg, C. P. (2008). The pace of morphological change: historical
452 transformation of skull shape in St Bernard dogs. *Proceedings of the Royal Society B:*
453 *Biological Sciences*, 275(1630), 71-76.
- 454 Dumoncel, J., Subsol, G., Durrleman, S., Bertrand, A., de Jager, E., Oettlé, A. C., ... &
455 Beaudet, A. (2020). Are endocasts reliable proxies for brains? A 3D quantitative comparison
456 of the extant human brain and endocast. *Journal of Anatomy*
- 457 Early, C. M., Iwaniuk, A. N., Ridgely, R. C., & Witmer, L. M. (2020). Endocast structures are
458 reliable proxies for the sizes of corresponding regions of the brain in extant birds. *Journal of*
459 *Anatomy*.
- 460 Edamoto, M., Kuroda, Y., Yoda, M., Kawaai, K., & Matsuo, K. (2019). Trans-pairing between
461 osteoclasts and osteoblasts shapes the cranial base during development. *Scientific reports*,
462 9(1), 1-11.
- 463 Enlow, D. H. (1962). A study of the post-natal growth and remodeling of bone. *American*
464 *Journal of Anatomy*, 110(2), 79-101.
- 465 Green, R. M., Fish, J. L., Young, N. M., Smith, F. J., Roberts, B., Dolan, K., ... & Roseman,
466 C. C. (2017). Developmental nonlinearity drives phenotypic robustness. *Nature*
467 *communications*, 8(1), 1970.
- 468 Goswami, A., Binder, W. J., Meachen, J., & O'Keefe, F. R. (2015). The fossil record of
469 phenotypic integration and modularity: A deep-time perspective on developmental and
470 evolutionary dynamics. *Proceedings of the National Academy of Sciences*, 112(16), 4891-
471 4896.
- 472 Gould, S. J. (2002). *The structure of evolutionary theory*. Harvard University Press.
- 473 Guo, T., Jou, W., Chanturiya, T., Portas, J., Gavrilova, O., & McPherron, A. C. (2009).
474 Myostatin inhibition in muscle, but not adipose tissue, decreases fat mass and improves
475 insulin sensitivity. *PloS one*, 4(3), e4937.

- 476 Hayashi, Y., Mikawa, S., Ogawa, C., Masumoto, K., Katou, F., & Sato, K. (2018). Myostatin
477 expression in the adult rat central nervous system. *Journal of chemical neuroanatomy*, *94*,
478 125-138.
- 479 Jarvis, D. A., Finney, C. R., & Griffiths, P. D. (2019). Normative volume measurements of the
480 fetal intra-cranial compartments using 3D volume in utero MR imaging. *European radiology*,
481 *29*(7), 3488-3495.
- 482 Jeffery, N. (2003). Brain expansion and comparative prenatal ontogeny of the non-hominoid
483 primate cranial base. *Journal of human evolution*, *45*(4), 263-284.
- 484 Jeffery, N. (2005). Cranial base angulation and growth of the human fetal pharynx. *The*
485 *Anatomical Record Part A: Discoveries in Molecular, Cellular, and Evolutionary Biology: An*
486 *Official Publication of the American Association of Anatomists*, *284*(1), 491-499.
- 487 Jeffery, N., Davies, K., Köckenberger, W., & Williams, S. (2007). Craniofacial growth in fetal
488 *Tarsius bancanus*: brains, eyes and nasal septa. *Journal of anatomy*, *210*(6), 703-722.
- 489 Jeffery, N., & Mendias, C. (2014). Endocranial and masticatory muscle volumes in
490 myostatin-deficient mice. *Royal Society open science*, *1*(4), 140187.
- 491 Jeffery, N., & Spoor, F. (2002). Brain size and the human cranial base: a prenatal
492 perspective. *American journal of physical anthropology*, *118*(4), 324.
- 493 Jeffery, N., & Spoor, F. (2004). Ossification and midline shape changes of the human fetal
494 cranial base. *American Journal of Physical Anthropology*, *123*(1), 78-90.
- 495 Jeffery, N. S., Stephenson, R. S., Gallagher, J. A., Jarvis, J. C., & Cox, P. G. (2011). Micro-
496 computed tomography with iodine staining resolves the arrangement of muscle fibres.
497 *Journal of biomechanics*, *44*(1), 189-192.
- 498 Kappers, C. A. (1932). The David Ferrier Lecture: On Some Correlations between Skull and
499 Brain. *Philosophical Transactions of the Royal Society of London. Series B, Containing*
500 *Papers of a Biological Character*, 391-429.
- 501 Klingenberg, C. P. (2008). Morphological integration and developmental modularity. *Annual*
502 *review of ecology, evolution, and systematics*, *39*, 115-132.
- 503 Klingenberg, C. P. (2014). Studying morphological integration and modularity at multiple
504 levels: concepts and analysis. *Philosophical Transactions of the Royal Society B: Biological*
505 *Sciences*, *369*(1649), 20130249.
- 506 Klingenberg, C. P. (2016). Size, shape, and form: concepts of allometry in geometric
507 morphometrics. *Development genes and evolution*, *226*(3), 113-137.
- 508 Kong, X., Yao, T., Zhou, P., Kazak, L., Tenen, D., Lyubetskaya, A., ... & Liu, T. (2018).
509 Brown adipose tissue controls skeletal muscle function via the secretion of myostatin. *Cell*
510 *metabolism*, *28*(4), 631-643.
- 511 Kyriakopoulou, V., Vatansever, D., Davidson, A., Patkee, P., Elkommos, S., Chew, A., ... &
512 Fox, M. (2017). Normative biometry of the fetal brain using magnetic resonance imaging.
513 *Brain Structure and Function*, *222*(5), 2295-2307.

- 514 Lahti, D. C., Johnson, N. A., Ajie, B. C., Otto, S. P., Hendry, A. P., Blumstein, D. T., ... &
515 Foster, S. A. (2009). Relaxed selection in the wild. *Trends in ecology & evolution*, 24(9), 487-
516 496.
- 517 Laland, K. N., Uller, T., Feldman, M. W., Sterelny, K., Müller, G. B., Moczek, A., ... & Odling-
518 Smee, J. (2015). The extended evolutionary synthesis: its structure, assumptions and
519 predictions. *Proceedings of the Royal Society B: Biological Sciences*, 282(1813), 20151019.
- 520 Lee, C., Richtsmeier, J. T., & Kraft, R. H. (2019). A coupled reaction–diffusion–strain model
521 predicts cranial vault formation in development and disease. *Biomechanics and modeling in*
522 *mechanobiology*, 1-15.
- 523 Lesciotto, K. M., & Richtsmeier, J. T. (2019). Craniofacial skeletal response to
524 encephalization: How do we know what we think we know?. *American journal of physical*
525 *anthropology*, 168, 27-46.
- 526 Lieberman, D. E., Ross, C. F., & Ravosa, M. J. (2000). The primate cranial base: ontogeny,
527 function, and integration. *American Journal of Physical Anthropology: The Official*
528 *Publication of the American Association of Physical Anthropologists*, 113(S31), 117-169.
- 529 Maas, S. A., Ellis, B. J., Ateshian, G. A., & Weiss, J. A. (2012). FEBio: finite elements for
530 biomechanics. *Journal of biomechanical engineering*, 134(1), 011005.
- 531 McPherron, A. C., & Lee, S. J. (2002). Suppression of body fat accumulation in myostatin-
532 deficient mice. *The Journal of clinical investigation*, 109(5), 595-601.
- 533 Mendias, C. L., Marcin, J. E., Calerdon, D. R., & Faulkner, J. A. (2006). Contractile
534 properties of EDL and soleus muscles of myostatin-deficient mice. *Journal of applied*
535 *physiology*, 101(3), 898-905.
- 536 Michejda, M. (1972). The role of basicranial synchondroses in flexure processes and
537 ontogenetic development of the skull base. *American Journal of Physical Anthropology*,
538 37(1), 143-150.
- 539 Morand, O., Chanez, C., Masson, M., Dumont, O., Flexor, M. A., Baumann, N., & Bourre, J.
540 M. (1981). Intrauterine growth retardation (malnutrition by vascular ligation) induces
541 modifications in fatty acid composition of neurons and oligodendrocytes. *Journal of*
542 *neurochemistry*, 37(4), 1057-1060.
- 543 Moss, M. L. & Young, R. W. A functional approach to craniology. *American Journal of*
544 *Physical Anthropology* 281-92 (1960)
- 545 Mouisel, E., Relizani, K., Mille-Hamard, L., Denis, R., Hourdé, C., Agbulut, O., ... & Garcia, L.
546 (2014). Myostatin is a key mediator between energy metabolism and endurance capacity of
547 skeletal muscle. *American Journal of Physiology-Regulatory, Integrative and Comparative*
548 *Physiology*, 307(4), R444-R454.
- 549 Murren, C. J., Auld, J. R., Callahan, H., Ghalambor, C. K., Handelsman, C. A., Heskell, M. A.,
550 & Pfennig, D. W. (2015). Constraints on the evolution of phenotypic plasticity: limits and
551 costs of phenotype and plasticity. *Heredity*, 115(4), 293.

- 552 Neaux, D., Gilissen, E., Coudyzer, W., & Guy, F. (2015). Integration between the face and
553 the mandible of Pongo and the evolution of the craniofacial morphology of orangutans.
554 *American journal of physical anthropology*, 158(3), 475-486.
- 555 Neubauer, G. (1925). Experimentelle Untersuchungen über die Beeinflussung der
556 Schädelform. *Zeitschrift für Morphologie und Anthropologie*, (H. 3), 411-442.
- 557 Oladipupo, L., Wood, B., Mano, N., Hughes, G., Reynolds, R., Vinyard, C., ... & Smith, T.
558 (2020). Development of basicranium in cotton-top tamarin compared to the development of
559 basicranium in bushbabies: Role of synchondroses and brain growth. *The FASEB Journal*,
560 34(S1), 1-1.
- 561 Ploquin, C., Chabi, B., Fouret, G., Vernus, B., Feillet-Coudray, C., Coudray, C., ... &
562 Ramonatxo, C. (2012). Lack of myostatin alters intermyofibrillar mitochondria activity,
563 unbalances redox status, and impairs tolerance to chronic repetitive contractions in muscle.
564 *American journal of physiology-Endocrinology and metabolism*, 302(8), E1000-E1008.
- 565 Ross, C. F. & Henneberg, M. (1995). Basicranial flexion, relative brain size and facial
566 kyphosis in *Homo sapiens* and some fossil hominids. *American Journal of Physical*
567 *Anthropology* **98**, 575-593.
- 568 Ross, C. F., & Kirk, E. C. (2007). Evolution of eye size and shape in primates. *Journal of*
569 *Human Evolution*, 52(3), 294-313.
- 570 Ross, C. F. & Ravosa, M. J. (1993). Basicranial flexion, relative brain size, and facial
571 kyphosis in nonhuman primates. *American Journal of Physical Anthropology* **91**, 305-324.
- 572 Schafer, M. J., & LeBrasseur, N. K. (2019). The influence of GDF11 on brain fate and
573 function. *GeroScience*, 41(1), 1-11.
- 574 Singleton, M. (2013) Primate Cranial Diversity. *Nature Education Knowledge* 4(12):1
- 575 Stedman, H. H., Kozyak, B. W., Nelson, A., Thesier, D. M., Su, L. T., Low, D. W., ... &
576 Mitchell, M. A. (2004). Myosin gene mutation correlates with anatomical changes in the
577 human lineage. *Nature*, 428(6981), 415.
- 578 Stewart, S., Darwood, A., Masouros, S., Higgins, C., & Ramasamy, A. (2020).
579 Mechanotransduction in osteogenesis. *Bone & Joint Research*, 9(1), 1-14.
- 580 Vecchione, L., Miller, J., Byron, C., Cooper, G. M., Barbano, T., Cray, J., ... & Mooney, M. P.
581 (2010). Age-related changes in craniofacial morphology in GDF-8 (myostatin)-deficient mice.
582 *The Anatomical Record: Advances in Integrative Anatomy and Evolutionary Biology*, 293(1),
583 32-41.
- 584 Vecchione, L., Byron, C., Cooper, G. M., Barbano, T., Hamrick, M. W., Sciote, J. J., &
585 Mooney, M. P. (2007). Craniofacial morphology in myostatin-deficient mice. *Journal of dental*
586 *research*, 86(11), 1068-1072.
- 587 Veneziano, A., Meloro, C., Irish, J. D., Stringer, C., Profico, A., & De Groote, I. (2018).
588 Neuromandibular integration in humans and chimpanzees: Implications for dental and
589 mandibular reduction in Homo. *American journal of physical anthropology*, 167(1), 84-96.

590 Vickerton, P., Jarvis, J., & Jeffery, N. (2013). Concentration-dependent specimen shrinkage
591 in iodine-enhanced micro CT. *Journal of anatomy*, 223(2), 185-193.

592 Vincent, T. L., & Wann, A. K. (2019). Mechanoadaptation: articular cartilage through thick
593 and thin. *The Journal of physiology*, 597(5), 1271-1281.

594 Weidenreich, F. (1941). The brain and its role in the phylogenetic transformation of the
595 human skull. *Transactions of the American Philosophical Society*, 320-442.

596 Weiss, P. (1933). Functional adaptation and the role of ground substances in development.
597 *The American Naturalist*, 67(711), 322-340.

598 Williams, S. H., Lozier, N. R., Montuelle, S. J., & de Lacalle, S. (2015). Effect of postnatal
599 myostatin inhibition on bite mechanics in mice. *Plos one*, 10(8), e0134854.

600 Wolff, J. (1893). Das gesetz der transformation der knochen. *DMW-Deutsche Medizinische*
601 *Wochenschrift*, 19(47), 1222-1224.

602 Zheng, J., Payne, J. L., & Wagner, A. (2019). Cryptic genetic variation accelerates evolution
603 by opening access to diverse adaptive peaks. *Science*, 365(6451), 347-353.

604 Zelditch, M. L., & Fink, W. L. (1996). Heterochrony and heterotopy: stability and innovation in
605 the evolution of form. *Paleobiology*, 22(2), 241-254.

606 Zollikofer, C. P. E., & Ponce De León, M. S. (2004). Kinematics of cranial ontogeny:
607 heterotopy, heterochrony, and geometric morphometric analysis of growth models. *Journal*
608 *of Experimental Zoology Part B: Molecular and Developmental Evolution*, 302(3), 322-340.

609 Zollikofer CPE, Bienvenu T, and Ponce de León MS. 2017. Effects of cranial integration on
610 hominid endocranial shape. *Journal of anatomy* 230(1):85-105.

611
612
613

Tables

614
615
616

Table 1. Computationally driven changes of muscle and endocranial volume based on a 28day control (+/+) mouse mesh.

Simulation ID	Δ Muscle Volume %	Δ Endocranial Volume %
S_{+/+}	0	0
S_{-/-}	+17	-7
M₊₁₀	+10	0
M₊₁₇	+17	0
M₊₂₃	+23	0
E₊₁₁	0	+11
E₊₂₀	0	+20
E₊₃₀	0	+30
M₊₆E₊₅	+6	+5
M₊₁₀E₊₉	+10	+9
M₊₂₇E₊₂₁	+27	+21

617 S_{+/+} and S_{-/-} represent the +/+ and -/- conditions, respectively. Remaining models simulate
618 the combined and separate effects of muscle and endocranial expansion

619

620

621

622

623 Table 2. Myostatin $-/-$ versus $+/+$ canonical variate analysis (1000 permutations) based on
624 size corrected Procrustes data.

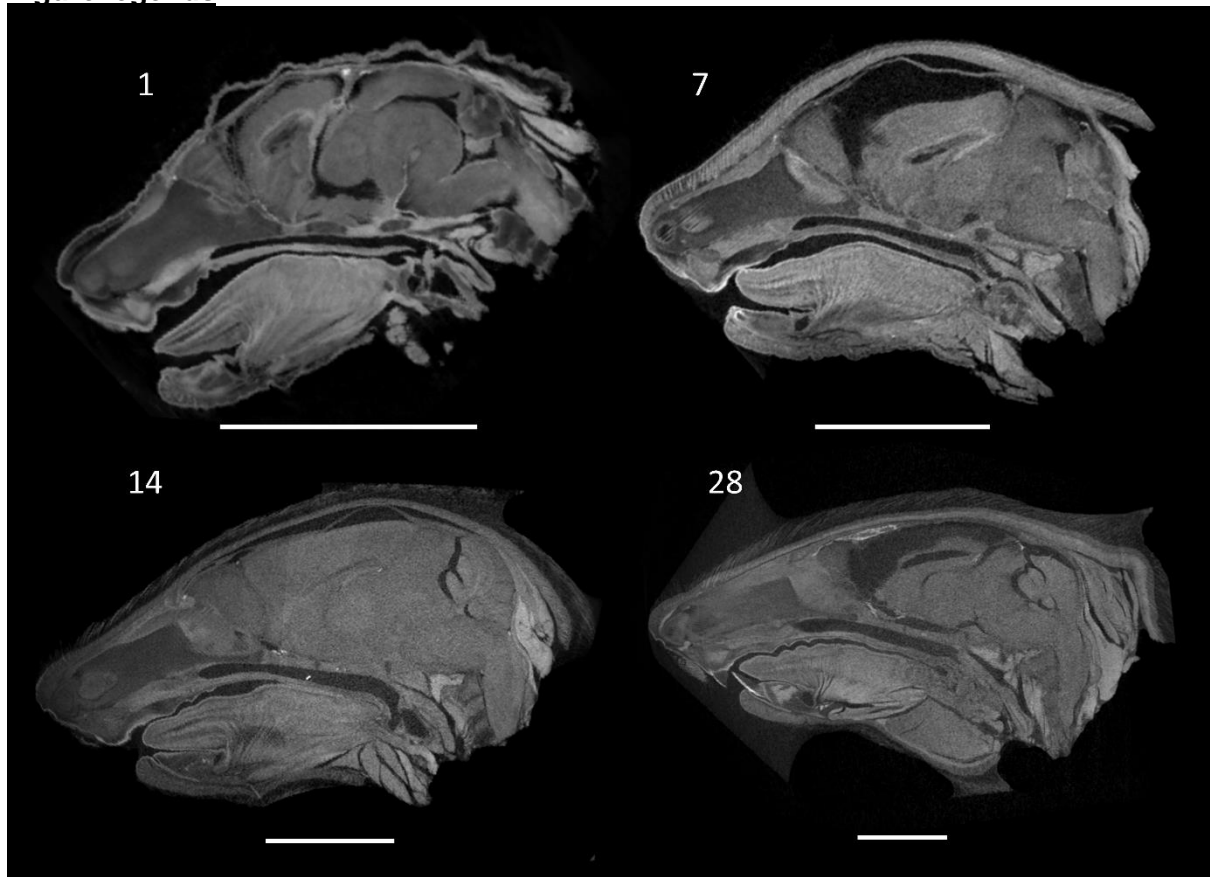
Age Grp (days)	N	Procrustes Distance †	Permutation p-value
1	12	0.0256	0.0101
7	12	0.0189	0.0008
14	12	0.0273	0.0014
28	12	0.0271	0.0020

625 † distance between $+/+$ and $-/-$ mice

626

627

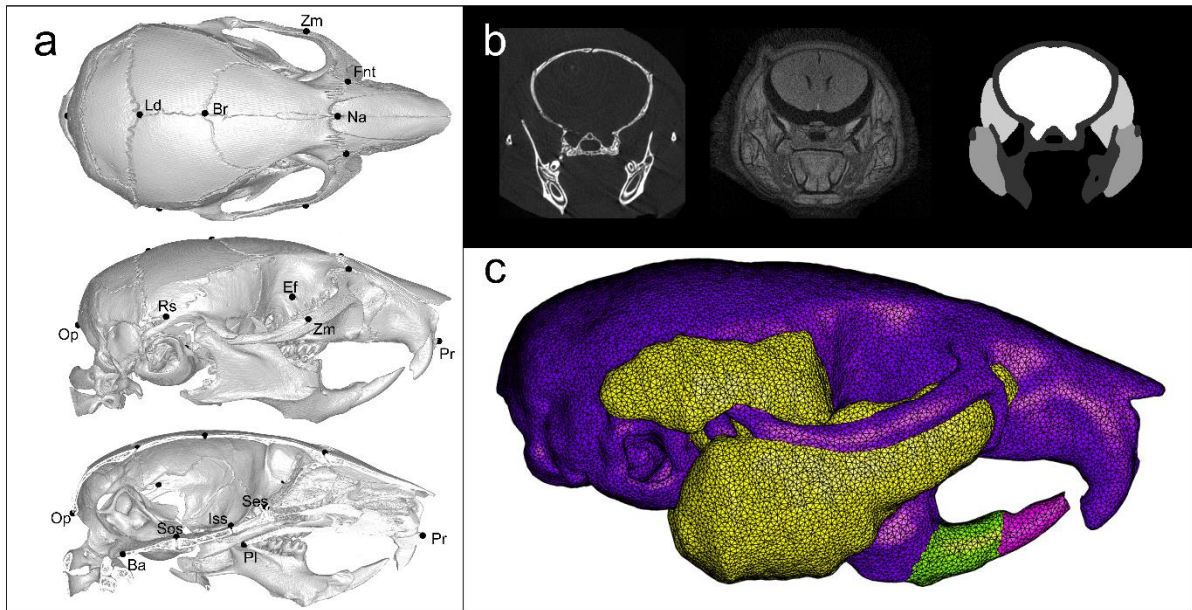
Figure legends



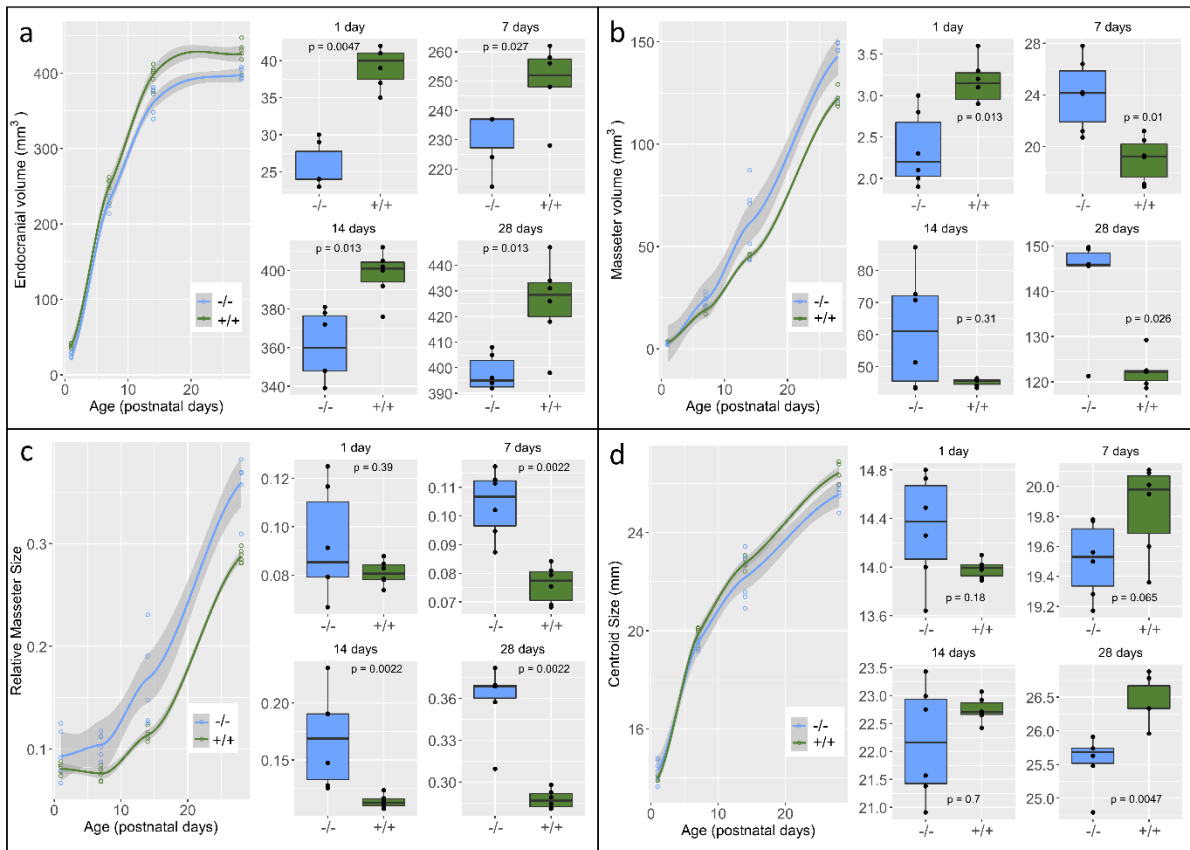
628

629

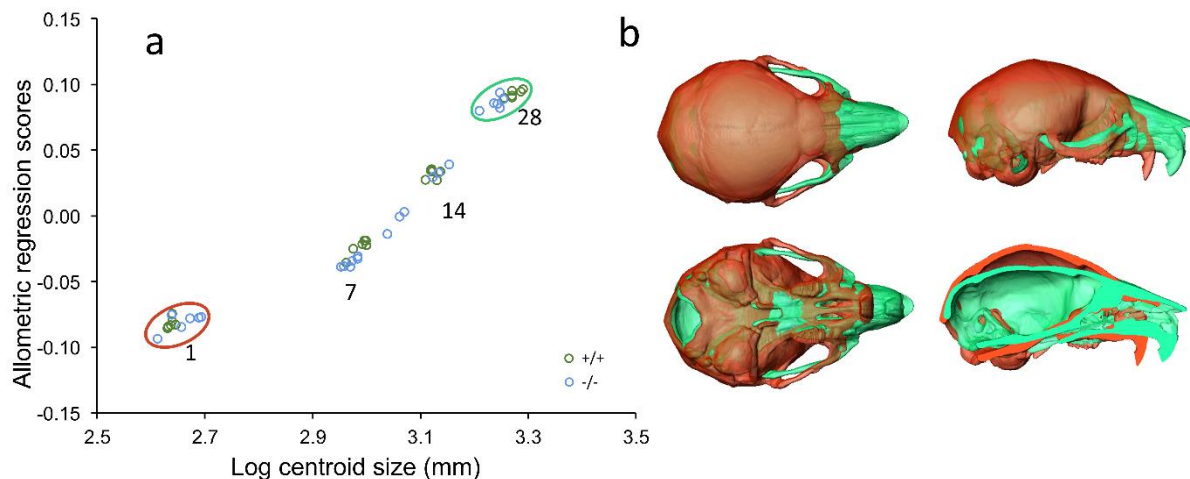
630 **Figure 1.** Example I_2KI enhanced microCT images reformatted along the midsagittal plane
631 at postnatal day 1, 7, 14 and 28. Scale bar 5mm.



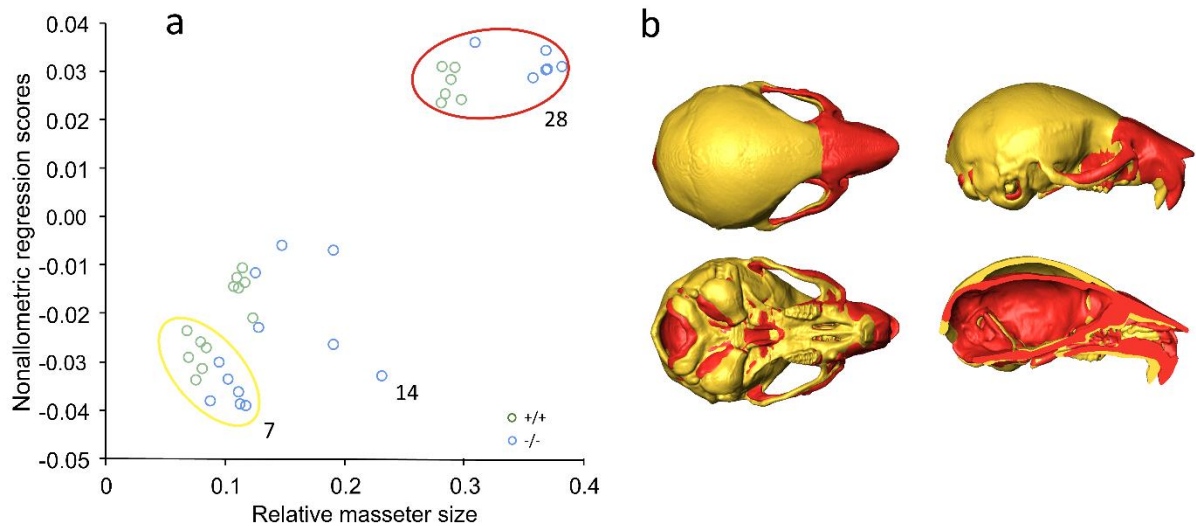
632
 633 **Figure 2.** Reformatted and rendered image data showing: **a)** from top to bottom, dorsal,
 634 lateral and midline views of the landmark configuration superimposed on 3D isosurfaces (Ba,
 635 basion; Br, bregma; Ef, ethmoid foramen; Fnt, junction between zygomatic, frontal and
 636 premaxillary bones; Iss, intersphenoidal synchondrosis; Ld, lambda; Na, nasion; Op,
 637 opisthion; Pl, posteriormost point of palatine suture; Pr, prosthion; Rs, recess above post-
 638 tympanic hook; Ses, spheno-ethmoidal synchondrosis; Sos, spheno-occipital
 639 synchondrosis; Zm, dorsal margin of zygomaticomaxillary suture); **b)** from left to right,
 640 standard coronal microCT scan, I_2KI enhanced coronal microCT scan and the corresponding
 641 composite label mapping; **c)** tetrahedral 3D mesh of mouse M1C1 used to create
 642 simulations (bone, purple; muscle, yellow; endocranium, not shown; green & pink,
 643 constraint).
 644



645
 646 **Figure 3.** Bivariate plots with LOESS fits against age (standard error, grey) and boxplot
 647 comparisons between +/+ (green) and -/- (blue) mice at 1, 7, 14 and 28 postnatal days for
 648 measures of **a)** masseter volume; **b)** endocranial volume; **c)** relative masseter size
 649 (masseter volume/endocranial volume); **d)** centroid size. Boxplots show the 25th, 50th & 75th
 650 percentiles with hinges for datum points within 1.5 times the percentile range (p-values are
 651 for Wilcoxon tests between +/+ and -/- means).
 652

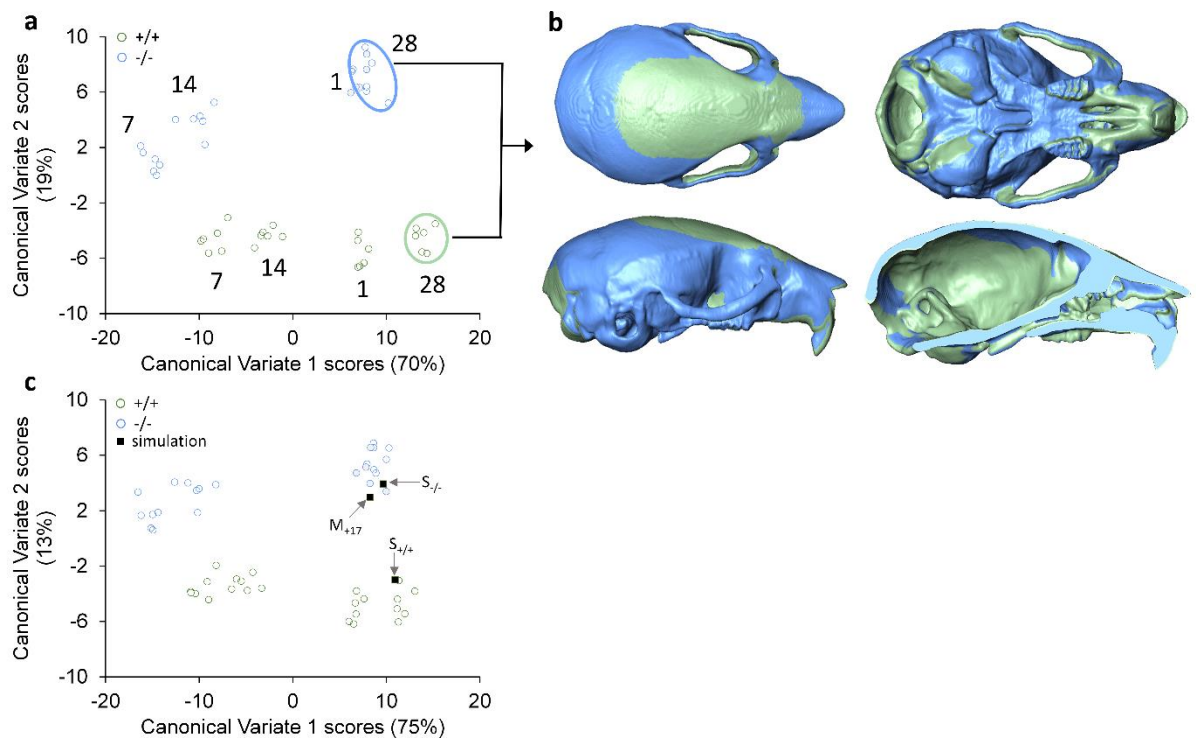


653
 654 **Figure 4.** Size (allometric) related changes of craniofacial shape: **a)** bivariate plot of
 655 regression scores from the Procrustes form space against log centroid size illustrating the
 656 common allometric trend through the age groups of -/- and +/+ mice; **b)** surface renderings
 657 representing the allometric trend from the mean day 1 mouse shape (rose) to the mean day
 658 28 shape (green).
 659
 660



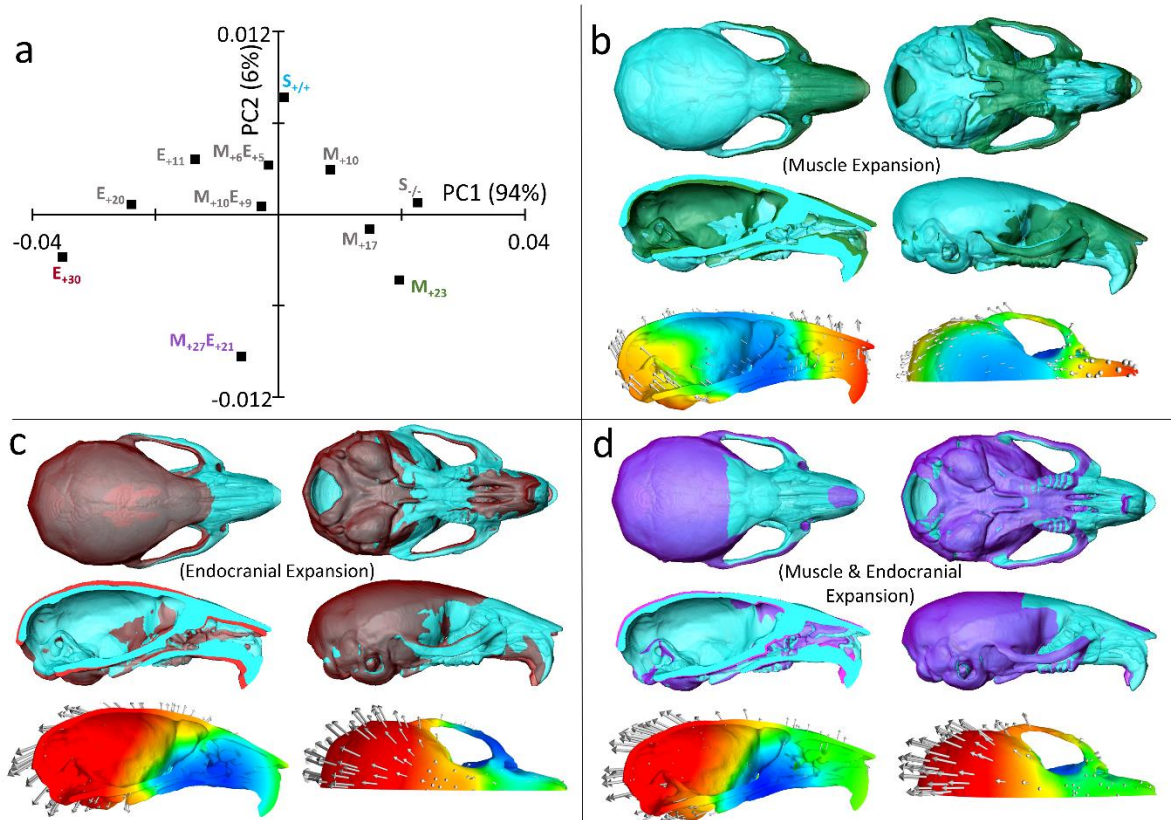
661
662
663
664
665
666
667
668

Figure 5. Size corrected (nonallometric) related changes of craniofacial shape in relation to relative masseter size from 7 to 28 days: **a)** bivariate plot of nonallometric regression scores against relative masseter size, accounting for 48% of the size corrected shape variation; **b)** surface renderings representing size corrected shape variation associated with increases of relative masseter size from 7 (yellow) to 28 days (red).



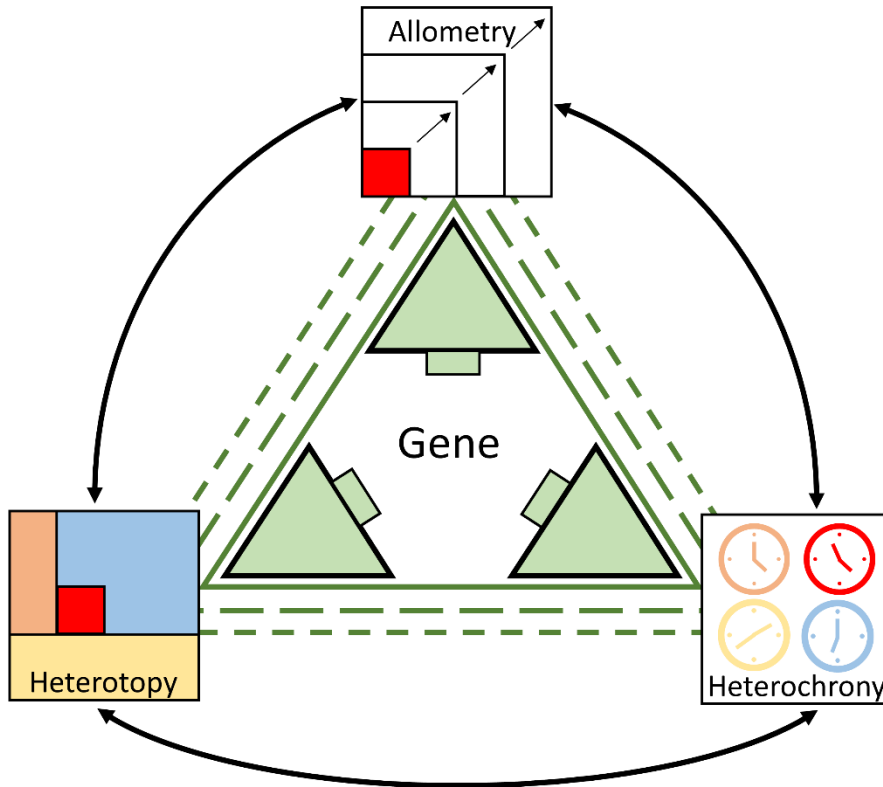
669
670
671
672
673
674
675

Figure 6. Nonallometric differences between -/- and +/+ mice: **a)** Plot of canonical variate scores showing the partial separation of age groups along CV1 and separation of -/- & +/+ mice along CV2; **b)** 3D renderings representing nonallometric shape differences between MSTN-/- and +/+ mice at day 28 based on a discriminative function; **c)** plot of canonical variate scores including simulations (refer to Table 1 for abbreviations).



676
 677
 678
 679
 680
 681
 682
 683
 684
 685
 686
 687
 688
 689

Figure 7. Soft-tissue expansion simulations; **a)** plot showing the distribution of simulated skulls along principal components 1 and 2 of the shape space (refer to Table 1 for abbreviations). Note that simulated muscle (e.g. M_{+17}) expansions are primarily distributed along positive PC1 scores whereas simulated endocranial expansions (e.g. E_{+20}) fall along the negative PC1 scores. Combined muscle and endocranial expansions (e.g. $M_{+27}E_{+21}$) fall along PC2; **b-d)** 3D renderings of the corresponding shape changes (± 0.05 PC scale factor) from the mean control shape ($S_{+/+}$, light blue) to the simulated shape (**b**, green represents expanded muscle [M_{+23}]; **c**, rose represents expanded endocranium [E_{+30}]; **d**, purple represents combined expansion of muscle and endocranium [$M_{+27}E_{+21}$]). Accompanying colour mapped 3D renderings illustrate the corresponding mesh deformations (red, high deformation; blue, low deformation; arrows also indicate direction and magnitude [arrow length] of deformation).



690
 691 **Figure 8.** Diagrammatic representation of gene derived covariations of form manifested
 692 through heterochrony (timing), allometry (size) and heterotopy (location). As ontogeny
 693 progresses, these covariations lose coherence (broken green lines) and other sources (black
 694 lines) such as the competition for space between nearby enlarging structures (heterotopy-
 695 allometry) become more conspicuous.
 696